Computers and Concrete, *Vol. 21, No. 2 (2018) 219-229*
DOI: https://doi.org/10.12989/cac.2018.21.2.219

A modified RBSM for simulating the failure process of RC structures

Chao Zhao[1a], Xingu Zhong[*1,2], Bo Liu[1,3b], Xiaojuan Shu[2] and Mingyan Shen[2]

[1]School of Mechanics and Civil Engineering, China University of Mining and Technology (Beijing),
Ding No.11 Xueyuan Road, Haidian District, Beijing, China
[2]School of Civil Engineering, Hunan University of Science and Technology, Taoyuan Road, Yuhu District, Xiangtan, China
[3]State Key Laboratory of Deep Geomechanics and Underground Engineering,
No.16 Qinghua East Road, Haidian District, Beijing, China

(Received April 22, 2017, Revised December 18, 2017, Accepted December 23, 2017)

Abstract. In this paper, a modified rigid body spring model (RBSM) is proposed and used to analyze the damage and failure process of reinforced concrete (RC) structures. In the proposed model, the concrete is represented by an assembly of rigid blocks connected with a uniform distribution of normal and tangential springs to simulate the macroscopic mechanical behavior of concrete. Steel bars are evenly dispersed into rigid blocks as a kind of homogeneous axial material, and an additional uniform distribution of axial and dowel springs is defined to consider the axial stiffness and dowel action of steel bars. Perfect bond between the concrete and steel bars is assumed, and tension stiffening effect of steel bars is modeled by adjusting the constitutive relationship for the tensile reinforcement. Adjacent blocks are allowed to separate at the contact interface, which makes it convenient and easy to simulate the cracking process of concrete. The failure of the springs is determined by the Mohr-Coulomb type criterion with the tension and compression caps. The effectiveness of the proposed method is confirmed by elastic analyses of a cantilever beam under different loading conditions and failure analyses of a RC beam under two-point loading.

Keywords: reinforced concrete structures; failure process; rigid body spring model; cracks; bearing capacity

1. Introduction

Numerical simulation is an effective method to study the failure mechanism of RC structures. The failure process of a RC structure is often accompanied with the generation and propagation of cracks. Cracks not only induce discontinuity in the medium, but also cause stress redistribution and stiffness degradation in regions around cracks, which makes the failure process analysis of RC structures a complicated and difficult task (Long and Lee 2015, Long *et al*. 2013).

Finite Element Method (FEM) is the major numerical tool for the study of RC structures, and there have been many researches concerning the modeling of failure in the finite element method, which can be roughly divided into two categories: discrete and continuum approaches. In discrete approaches, cracks are modeled as strong discontinuities. Examples are the virtual crack closure technique (Carter *et al*. 2000) and the extended finite element method (Belytschko *et al*. 1996, Belytschko and Black 1999). A drawback of the first method is the need to specify the crack path a-priori. While the crack path may be arbitrary, calculation of the extended finite element method is time consuming. In continuum approaches, the discontinuity of the displacement field caused by the crack is spread across the element by changing the material constitutive equation. And the accuracy of numerical results greatly depends on the material constitutive models, especially for concrete. As for material models, the concrete damage plasticity models (Long and Lee 2015, Long *et al*. 2014) and other smeared crack models (Bernardi *et al*. 2015, Sirico *et al*. 2017, Vecchio and Shim 2004, Vecchio *et al*. 2004, Jin *et al*. 2005, Barzegar and Maddipudi 1997) are usually employed in continuum approaches to predict the concrete compression and tension behaviors.

As an alternative way, various discrete element methods have been intensively developed and widely applied to rock and concrete structures during last decades (Shi 1988, Shi 1994, Li *et al*. 2015, Guo and Zhao 2014, Burns and Hanley 2017). Discrete methods do not rely on the continuum assumption, which makes them efficient and convenient numerical tools to simulate the cracking process of structures. The rigid body spring method (RSBM) is one of such methods which was firstly proposed by Kawai (1977). In RBSM, a structure is considered as a series of rigid blocks connected with interface springs, as shown in Fig. 1(a). The displacements of an arbitrary point are completely determined by the centroidal displacements of blocks. Adjacent blocks are allowed to separate at the contact interface, which makes it convenient and easy to simulate the cracking process of structures, as shown in Fig. 1(b). Recently, theoretical research and project applications of RBSM mainly focus on brittle materials, such as rocks and plain concrete (Yao *et al*. 2016, Wang and Zhang 2009, Zhang *et al*. 2012), and very little, if any, published literatures describe the use of RBSM to analyze the failure

---

∗Corresponding author, Professor
E-mail: 464397070@qq.com
[a]Ph.D. Student
E-mail: 287832614@qq.com
[b]Professor
E-mail: liub@cumtb.edu.cn

http://www.techno-press.org/?journal=cac&subpage=8
ISSN: 1598-8198 (Print), 1598-818X (Online)

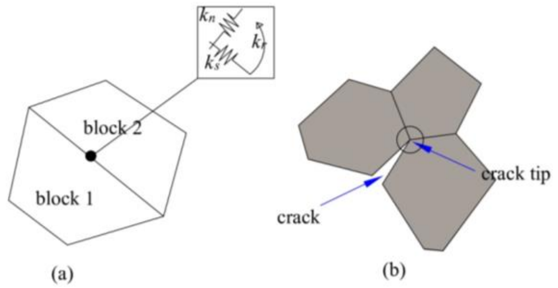

Fig. 1 The original RBSM: (a) contact model for the original RBSM; (b) crack modeling

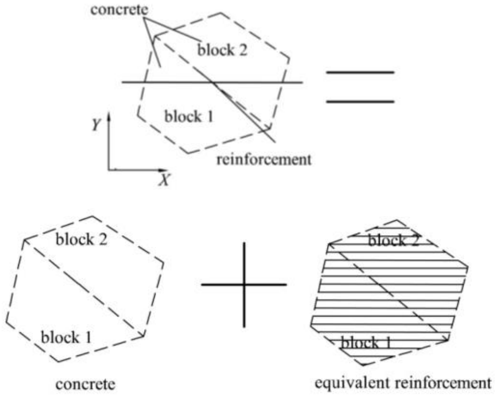

Fig. 2 The discrete model of the RC structure in the modified RBSM

process of RC structures.

In the present work, a modified RBSM is proposed and used to analyze the failure process of RC structures. In the proposed model, the concrete is represented by an assembly of rigid blocks, and the reinforcement is evenly dispersed into rigid blocks as a homogeneous axial material, as shown in Fig. 2. The blocks are connected with a uniform distribution of normal and tangential springs to simulate the macroscopic mechanical behavior of concrete, and another uniform distribution of axial and dowel springs is defined to consider the axial stiffness and dowel action of the reinforcement, as shown in Fig. 3. The failure of springs referred to the concrete is determined by the low tensile Mohr-Coulomb criterion, and the material nonlinearity and aggregate interlock are taken into consideration. The reinforcement is assumed to be an elastic-perfectly plastic material and identical in tension and compression, and perfect bond between the concrete and steel bars is assumed. The effectiveness of the proposed method is firstly verified by elastic analyses on a cantilever beam under different loading conditions, and then the method is applied to analyze the failure process of a RC beam under two-point loading.

2. Basic principles of the modified RBSM

2.1 Basic displacements of blocks

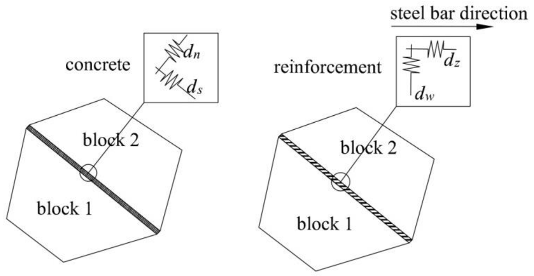

Fig. 3 Illustration of contact models for the modified RBSM

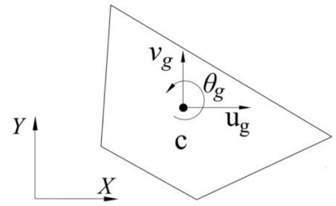

Fig. 4 Displacements of blocks

Each block has three degrees of freedom defined at its centroid, as shown in Fig. 4, and the displacements of an arbitrary point of a block are given by the following equation

$$\mathbf{u}=\begin{bmatrix}u & v\end{bmatrix}^{\mathbf{T}}=\mathbf{N}\bullet\mathbf{u_g} \tag{1}$$

$$\mathbf{N}=\begin{bmatrix}1 & 0 & (y_g-y)\\ 0 & 1 & (x-x_g)\end{bmatrix} \quad \mathbf{u_g}=\begin{bmatrix}u_g & v_g & \theta_g\end{bmatrix}^{\mathbf{T}} \tag{2}$$

where u, v are the translation displacements of a point of the block, respectively; $\mathbf{N}$, $\mathbf{u_g}$ are the shape function matrix and the centroidal displacements array of the block, respectively; u_g, v_g and θ_g are the translational displacements and the rotational displacement of the centroid of the block, respectively; x, y are the global coordinates of an arbitrary point of the block; x_g, y_g are the global coordinates of the centroid of the block.

2.2 The concrete model

The concrete is represented by an assembly of rigid blocks, which are connected with a uniform distribution of normal and tangential springs to simulate the macroscopic mechanical behavior of concrete. When adjacent blocks are separated or intruded at the interface, the deformation of the concrete springs at point A can be determined by the relative displacements between points A_1 and A_2, as shown in Fig. 5, and the mathematical expressions are as follows

$$\boldsymbol{\delta}_\mathbf{c}=\begin{bmatrix}\delta_n & \delta_s\end{bmatrix}^{\mathbf{T}}=-\mathbf{L_c}(\mathbf{u_1}-\mathbf{u_2}) \tag{3}$$

$$\mathbf{L_c}=\begin{bmatrix}\cos(\vec{\mathbf{n}},\vec{\mathbf{x}}) & \cos(\vec{\mathbf{n}},\vec{\mathbf{y}})\\ \cos(\vec{\mathbf{s}},\vec{\mathbf{x}}) & \cos(\vec{\mathbf{s}},\vec{\mathbf{y}})\end{bmatrix} \tag{4}$$

where δ_n, δ_s are the deformations of the normal and tangential springs at point A, respectively; $\mathbf{u}_1$ and $\mathbf{u}_2$ are the displacements of points A_1 and A_2, respectively; $\mathbf{L_c}$ is the coordinate-transformation matrix; $\vec{\mathbf{n}}$, $\vec{\mathbf{s}}$ are the normal and tangential vectors of the surface of the local system in

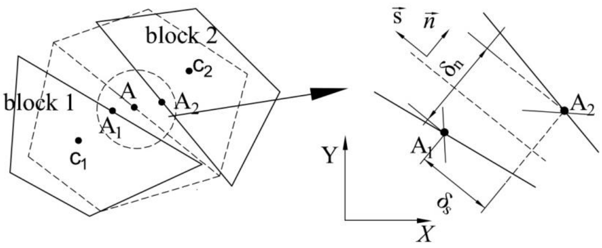

Fig. 5 The deformations of concrete springs at point A

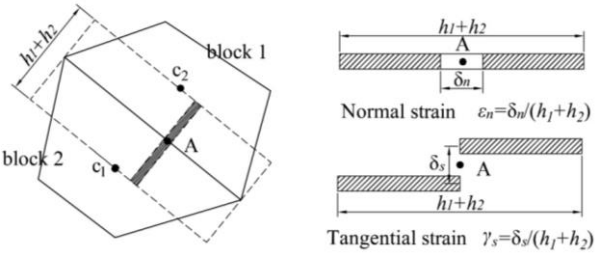

Fig. 6 The micro-strip of point A

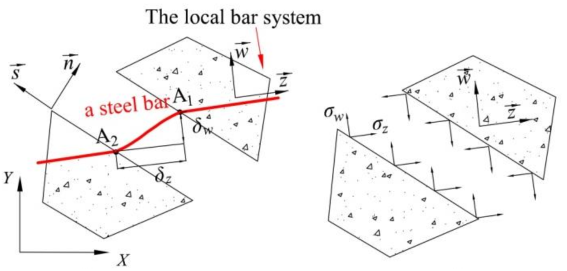

(a) (b)

Fig. 7 The adopted model for steel bars: (a) the local system for steel bars; (b) the static equivalent stresses

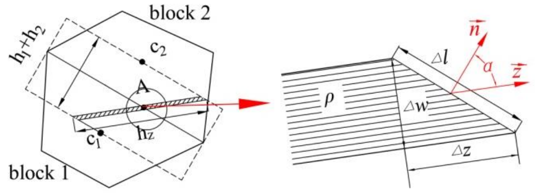

Fig. 8 The micro-strip for steel bars

Fig. 5. $\vec{x}$, $\vec{y}$ are the two unit vectors of the global coordinate system.

The equivalent concrete strains at point A are determined by the average deformations of the micro-strip shown in Fig. 6

$$\boldsymbol{\varepsilon}_\mathbf{c} = [\varepsilon_n \quad \gamma_s]^\mathbf{T} = \boldsymbol{\delta}_\mathbf{c}/(h_1+h_2) \tag{5}$$

where ε_n and γ_s denote the normal and tangential strains of concrete, respectively; h_1, h_2 are the vertical distances from the centroids of adjacent blocks to the interface, as shown in Fig. 6.

For plane stress problems, the local spring forces of one point on the interface are determined by the following equation

$$\mathbf{T}_\mathbf{c} = [\sigma_n \quad \tau_s]^\mathbf{T} = \mathbf{D}\boldsymbol{\varepsilon}_\mathbf{c} = \mathbf{D}_c\boldsymbol{\delta}_\mathbf{c} \tag{6}$$

where σ_n and τ_s denote the normal and tangential spring forces of concrete, respectively; **D** is the constitutive matrix of plane stress problems, and $\mathbf{D}_c$ is the matrix of concrete springs

$$\mathbf{D} = \begin{bmatrix} E_c & 0 \\ 0 & \dfrac{E_c}{2(1+\lambda)} \end{bmatrix} \tag{7}$$

$$\mathbf{D}_\mathbf{c} = \begin{bmatrix} d_n & 0 \\ 0 & d_s \end{bmatrix} = \begin{bmatrix} \dfrac{E_c}{h_1+h_2} & 0 \\ 0 & \dfrac{E_c}{(2+2\lambda)(h_1+h_2)} \end{bmatrix} \tag{8}$$

λ, E_c are Poisson's ratio and the elastic modulus of concrete, respectively; d_n and d_s are the stiffness of the normal and tangential springs in Fig. 3, respectively.

2.3 The reinforcement model

The forces in the steel bars due to the axial stiffness and dowel action are modeled in the local system of steel bars, as shown in Fig. 7(a), and then smeared so as to obtain the static equivalent stresses shown in Fig. 7(b).

Axial δ_z and transversal δ_w components in Fig. 7(a), with respect to the local bar system, of the steel bar displacement vector $\boldsymbol{\delta}_\mathbf{s}^*$ can be determined by the relative displacements between points A_1 and A_2,

$$\boldsymbol{\delta}_\mathbf{s}^* = [\delta_z \quad \delta_w]^\mathbf{T} = -\mathbf{L}_\mathbf{s}(\mathbf{u}_\mathbf{1} - \mathbf{u}_\mathbf{2}) \tag{9}$$

$$\mathbf{L}_s = \begin{bmatrix} \cos(\vec{\mathbf{z}},\vec{\mathbf{x}}) & \cos(\vec{\mathbf{z}},\vec{\mathbf{y}}) \\ \cos(\vec{\mathbf{w}},\vec{\mathbf{x}}) & \cos(\vec{\mathbf{w}},\vec{\mathbf{y}}) \end{bmatrix} \tag{10}$$

where δ_z, δ_w are the axial and dowel displacements of steel bars; $\mathbf{L}_s$ is the coordinate-transformation matrix between the local bar system and the global system; $\vec{\mathbf{z}}$, $\vec{\mathbf{w}}$ are the axial and transversal vectors of the local bar system.

The micro-strip in Fig. 8 is adopted, and the static equivalent stresses of steel bars at point A are expressed by the following equation

$$\mathbf{T}_\mathbf{s} = [\sigma_z \quad \sigma_w]^\mathbf{T} \tag{11}$$

where σ_z and σ_w denote the axial and dowel equivalent stresses of a steel bar, respectively.

The axial equivalent stress σ_z is determined by the following equation

$$\sigma_z = E_z \varepsilon_z \tag{12}$$

where ε_z is the average axial strain of the micro-strip; E_z is the elastic modulus of the reinforcement equivalent material, which can be obtained by the following equations

$$\varepsilon_z = \delta_z / h_z = \frac{|\cos\alpha|}{(h_1+h_2)}\delta_z \tag{13}$$

$$E_z = \frac{E_s \rho \Delta w}{\Delta l} = E_s \rho |\cos\alpha| \tag{14}$$

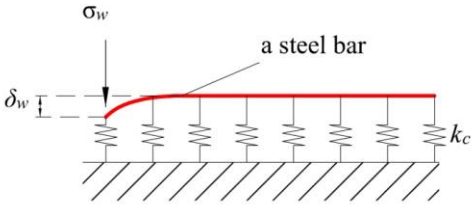

Fig. 9 The elastic foundation beam model

h_z is the calculation length of the micro-strip in Fig. 8; E_s is the secant elastic modulus of reinforcement; ρ is the average reinforcement ratio on a single rigid block; Δw is the width of the micro-strip, and Δl is the interface length covered by the micro-strip α is the included angle of the vector $\vec{\mathbf{z}}$ and vector $\vec{\mathbf{n}}$, as shown in Fig. 8.

As shown in Fig. 9, the dowel spring force σ_w is calculated by the elastic foundation beam theory (Tang and Xiang 2015, Long *et al.* 2014)

$$\sigma_w = n' K_d \delta_w \tag{15}$$

where n' is the equivalent amount of steel bars in each micro-strip, determined by the following equation

$$n' = \frac{\rho \Delta w}{A_s \Delta l} = \frac{\rho}{A_s}\left|\cos\alpha\right| \tag{16}$$

A_s is the sectional area of a single steel bar; K_d is the stiffness associated to dowel action

$$K_d = \lambda^3 E_s I$$

$$\lambda = \left[\frac{d_b \cdot k_c}{4 E_s I}\right]^{0.25} \qquad I = \pi d_b^4 / 64 \tag{17}$$

d_b is the diameter of steel bar; k_c is the concrete stiffness (foundation modulus), as shown in Fig. 9, which can be determined by the empirical formula proposed by Soroushian *et al.* (1987)

$$k_c = \frac{127 c_1 \sqrt{\left|f_c'\right|}}{d_b^{2/3}} \tag{18}$$

f_c' is the cylindrical compressive strength of concrete; c_1 is a coefficient ranging from 0.6 for a clear bar spacing of 0.025m to 1.0 for a larger bar spacing. (if f_c' in MPa and d_b in mm, k_c in MPa/mm).

Substituting Eqs. (12)-(15) into Eq. (11), the following equations are obtained

$$\mathbf{T_s} = \left[\sigma_z \quad \sigma_w\right]^{\mathbf{T}} = \mathbf{D_s}\boldsymbol{\delta}_\mathbf{s} \tag{19}$$

$$\mathbf{D}_s = \begin{bmatrix} d_z & 0 \\ 0 & d_w \end{bmatrix} = \begin{bmatrix} \dfrac{E_s \rho \left|\cos\alpha\right|^2}{\left(h_1 + h_2\right)} & 0 \\ 0 & \dfrac{K_d \rho \left|\cos\alpha\right|}{A_s} \end{bmatrix} \tag{20}$$

where d_z and d_w are the axial and normal spring stiffness of steel bars, respectively.

2.4 Virtual work equation of the modified RBSM

In the modified RBSM, the external work is stored in the springs between adjacent blocks. The overall energy balance equation of the modified RBSM is given as follows

$$\begin{aligned} &\sum_r \iint_{S_0^r} \frac{1}{2}\mathbf{T}_c^{(i)}\boldsymbol{\delta}_c^{(i)} ds + \sum_r \iint_{S_0^r} \frac{1}{2}\mathbf{T}_s^{(i)}\boldsymbol{\delta}_s^{(i)} ds \\ &= \sum_e \iiint_{\Omega^e} f_i \mathbf{u_i} d\Omega + \iint_{S_\sigma^e} \frac{1}{2}\mathbf{P_i u_i} ds \end{aligned} \tag{21}$$

where Ω^e is the domain of definition; S_σ^e is the force boundary; S_0^r is an interface in the domain; f_i, $\mathbf{P_i}$ are the gravity density of the material and the imposed loads, respectively. (Note: throughout the article, superscript (i) means the number of interfaces and subscript i means the number of blocks.)

After applying the principle of stationary potential energy, the following equilibrium equation is obtained

$$\left(\mathbf{K_c} + \mathbf{K_s}\right) \cdot \mathbf{U_g} = \mathbf{R} \tag{22}$$

where $\mathbf{U_g}$ is the global displacement array expressed as follows:

$$\mathbf{U_g} = \left[\mathbf{u_{g1}}, \quad \cdots, \quad \mathbf{u}_{\mathbf{g}i}, \quad \cdots, \quad \mathbf{u_{gn}}\right]^T \tag{23}$$

Subscript n in Eq. (23) represents the total number of rigid blocks; $\mathbf{R}$ is the equivalent load array defined by the following formula

$$\mathbf{R} = \sum_r \mathbf{C_i^T q} \qquad \mathbf{q} = \iiint_{\Omega^e} \mathbf{N_i^T} f_i d\Omega + \iint_{S_\sigma^e} \mathbf{N_i^T P_i} ds \tag{24}$$

$\mathbf{C_i}$ is the selection matrix of block i, and $\mathbf{u}_{\mathbf{g}i}=\mathbf{C_i U_g}$

$$\mathbf{C_i} = \begin{bmatrix} 0 & \cdots & 0 & a_{3i-2} & 0 & 0 & 0 & \cdots & 0 \\ 0 & \cdots & 0 & 0 & a_{3i-1} & 0 & 0 & \cdots & 0 \\ 0 & \cdots & 0 & 0 & 0 & a_{3i} & 0 & \cdots & 0 \end{bmatrix}_{3\times 3i}^{\mathbf{T}}$$

$$a_{3i-2} = a_{3i-1} = a_{3i} = 1 \tag{25}$$

$\mathbf{N_i}$ is the shape function of block i; $\mathbf{K_c}$ and $\mathbf{K_s}$ are the stiffness matrixes of the concrete and reinforcement, respectively

$$\mathbf{K_c} = \sum_r \mathbf{C^{(i)T}} \iint_{S_0^r} \mathbf{N^{(i)T} L_c^{(i)T} D_c^{(i)} L_c^{(i)} N^{(i)}} ds \mathbf{C^{(i)}} \tag{26}$$

$$\mathbf{K_s} = \sum_r \mathbf{C^{(i)T}} \iint_{S_0^r} \mathbf{N^{(i)T} L_s^{(i)T} D_s^{(i)} L_s^{(i)} N^{(i)}} ds \mathbf{C^{(i)}} \tag{27}$$

$$\mathbf{N^{(i)}} = \left[\mathbf{N}_{i1} \quad \mathbf{N}_{i2}\right] \quad \mathbf{C^{(i)}} = \left[\mathbf{C}_{i1} \quad -\mathbf{C}_{i2}\right] \tag{28}$$

Subscript $i1$, $i2$ in Eq. (28) represents the number of the two rigid blocks relevant to the interface i.

3. Material models for concrete and reinforcement

3.1 Material model for concrete under compression

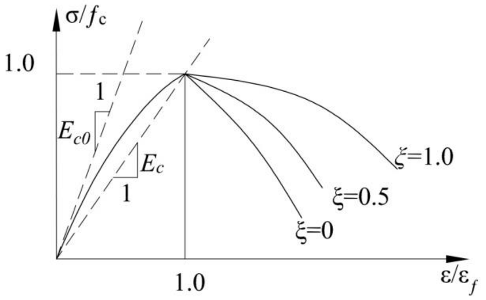

Fig. 10 Stress-strain curve for concrete

The material model for concrete under compression adopted herein is a modified uniaxial form of the 2D non-linear elastic model proposed by Bernardi, Cerioni, Michelini and Sirico (2015). The stress-strain curves shown in Fig. 10 are adopted in this paper. The mathematical expression is as follows

$$\frac{\sigma}{f_c}=\frac{\zeta\left(\varepsilon/\varepsilon_f\right)+\left(\xi-1\right)\left(\varepsilon/\varepsilon_f\right)^2}{1+\left(\zeta-2\right)\left(\varepsilon/\varepsilon_f\right)+\xi\left(\varepsilon/\varepsilon_f\right)^2}\qquad\left(\zeta=\frac{E_{c0}}{E_f}\right)\tag{29}$$

where σ and ε are positive when the concrete is in the compressive state; f_c is the uniaxial compressive strength of concrete; E_{c0} is the initial elastic modulus of concrete; $\varepsilon_f=2f_c/E_{c0}$ is the concrete strain corresponding to the stress f_c; $E_f=f_c/\varepsilon_f$ is the secant modulus corresponding to the stress f_c; ξ is a coefficient used to adjust the descending branch of the stress-strain curve, which is set to 1.0 in this paper.

The concrete secant elastic modulus E_c can be calculated as a function of the non-linearity index β through the the following equation

$$\begin{aligned}E_c&=\frac{1}{2}E_{c0}-\beta\left(\frac{1}{2}E_{c0}-E_f\right)+\\&\sqrt{\left(\frac{1}{2}E_{c0}-\beta\left(\frac{1}{2}E_{c0}-E_f\right)\right)^2+\beta E_f^2\left(\xi(1-\beta)-1\right)}\end{aligned}\tag{30}$$

The non-linearity index β depends on the proximity of the current stress point to its value at failure and can be evaluated through the expression

$$\beta=\frac{\sigma}{f_c}\qquad\sigma=\sqrt{\sigma_n^2+\tau_s^2}\tag{31}$$

where σ_n, τ_s are the normal and tangential spring forces of concrete determined by Eq. (6), respectively.

Crushing occur when the non-linearity index β is equal to or slightly greater than 1.0. The post-peak behaviour is then governed by the following equation

$$\begin{aligned}E_c&=\frac{1}{2}E_{c0}-\beta\left(\frac{1}{2}E_{c0}-E_f\right)-\\&\sqrt{\left(\frac{1}{2}E_{c0}-\beta\left(\frac{1}{2}E_{c0}-E_f\right)\right)^2+\beta E_f^2\left(\xi(1-\beta)-1\right)}\end{aligned}\tag{32}$$

which is formally identical to Eq. (30), but has a negative sign before the term under square root.

It has been experimentally observed that, in presence of compressive stresses, concrete tends firstly to compact and subsequently to expand after the appearance of micro cracks. To reproduce this behaviour, Poisson's ratio λ is expressed as a function of the non-linearity index and properly adjusted during the analysis, according to Ottosen (1980). In more detail, λ is kept fixed until β reaches a limit value β_a equal to 0.8, and afterwards it is updated by applying the following relation, representing a quarter of an ellipse

$$\lambda=\lambda_f-\left(\lambda_f-\lambda_0\right)\sqrt{1-\left(\frac{\beta-\beta_a}{1-\beta_a}\right)^2}\tag{33}$$

where λ_0 indicates the initial value of Poisson coefficient (assumed equal to 0.2), while λ_f represents its secant value at peak (approximately equal to 0.36).

3.2 Material model for concrete under tension

The concrete under tension behaves linearly elastic up to the tensile strength, then the stress-strain relationship exhibits strain softening until cracking, as shown in Fig. 11. The fracture energy can be introduced to define the softening branch. Introducing the damage parameter ω, the tension softening curve is defined by (Saito and Hikosaka 1999)

$$\sigma_n=\left(1-\omega\right)E_{c0}\varepsilon_n\tag{34}$$

where

$$\omega=\begin{cases}0 & \left(\varepsilon\le\varepsilon_t\right)\\ 1-\dfrac{\varepsilon_t}{\varepsilon_n}\exp\left[-\dfrac{\kappa}{\varepsilon_{tu}}\left(\varepsilon_n-\varepsilon_t\right)\right] & \left(\varepsilon>\varepsilon_t\right)\end{cases}\tag{35}$$

where ε_n is the normal strain of concrete determined by Eq. (5); $\varepsilon_t=f_t/E_{c0}$, and f_t is the tensile strength. The damage parameter ω represents the degree of damage and varies from 0 (no damage) up to 1 (complete damage). The constant parameter κ is set to 5. The ultimate strain ε_{tu}, where the stress is assumed to be zero, is approximately calculated by the following equation

$$\varepsilon_{tu}=\kappa\left(\frac{G_f}{f_t\left(h_1+h_2\right)}-\frac{f_t}{2E_{c0}}\right)\tag{36}$$

where G_f is the fracture energy which represents the amount of energy consumed to create a crack of one unit area. h_1 and h_2 are the vertical distances from the centroids of adjacent blocks to the interface.

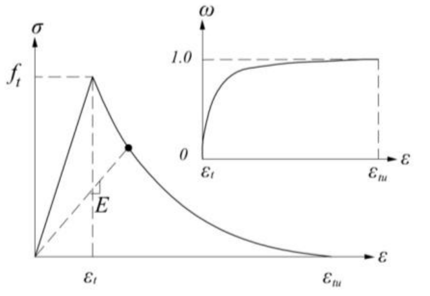

Fig. 11 Stress-strain curve for concrete

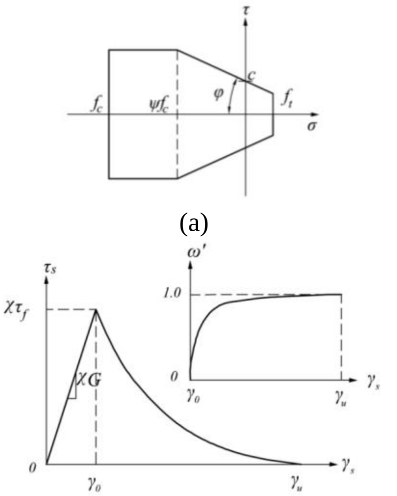

(a)

(b)

Fig. 12 Shear transferring model for concrete: (a) Mohr-Coulomb criterion for shear spring; (b) shear softening model for cracked interfaces

Poisson's ratio λ of concrete under tension is equal to λ_0 until the tensile stress reaches the tensile strength, then it turns to λ_f.

3.3 Shear transferring model for concrete after cracking

Tangential spring d_s represents the shear transferring mechanism of concrete. The shear strength is assumed to follow the Mohr-Coulomb type criterion with the tension and compression caps, as shown in Fig. 12(a) (Saito and Hikosaka 1999). That is

$$\begin{cases} \sigma_n \le f_c \\ \sigma_n \ge f_t \\ |\tau_s| \ge \tau_f \end{cases} \tag{37}$$

Where

$$\tau_f = \begin{cases} c - \sigma_n \tan\varphi & (\sigma_n \ge \psi f_c) \\ c - \psi f_c \tan\varphi & (\sigma_n < \psi f_c) \end{cases} \tag{38}$$

f_c is the uniaxial compressive strength of concrete; f_t is the uniaxial tensile strength of concrete; c and φ are the cohesion and internal friction angle, respectively; ψ is a constant parameter and equal to 0.5.

After the shear stress reaches the yield strength, a softening branch with the same softening rate as that of the tension softening model is assumed (Saito and Hikosaka 1999), as shown in Fig. 12(b). That is

$$\tau_s = (1-\omega')\chi G\gamma_s \qquad G = \frac{E_c}{2(1+\lambda)} \tag{39}$$

where

$$\omega' = \begin{cases} 0 & (\gamma_s \le \gamma_0) \\ 1 - \dfrac{\gamma_0}{\gamma_s}\exp\left[-\dfrac{\kappa}{\gamma_u}(\gamma_s - \gamma_0)\right] & (\gamma_s > \gamma_0) \end{cases} \tag{40}$$

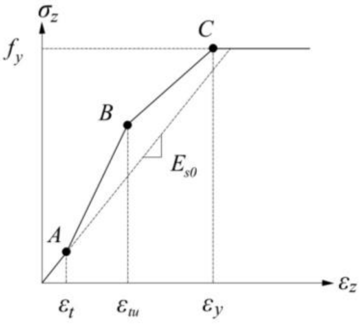

Fig. 13 Stress-strain relation for reinforcing steel

in which γ_s is the tangential strain of concrete determined by Eq. (5), and $\gamma_0=\tau_f/G$; ω' represents the degree of damage as the parameter ′ of the tension softening model; γ_u is the ultimate tangential strain of concrete, which is set to 4000μ in this paper.

The parameter χ is introduced to take account of the effect of concrete aggregate interlock, which is set to 1-ω and varies from 1 (no damage) down to 0 (complete damage), but the constant parameter κ is adjusted to 0.3 in order to provide an approximation to the shear stiffness reduction proposed by Aoyagi and Yamada (1983).

Finally, when cracks arise in concrete, the original concrete stiffness matrix Eq. (8) is replaced by

$$\mathbf{D_c} = \begin{bmatrix} d_n & 0 \\ 0 & (1\text{-}\omega')\chi d_s \end{bmatrix} \tag{41}$$

3.4 Material model for steel reinforcing bars

Steel bars are assumed to be an elastic-perfectly plastic material model which is identical in tension and compression. In the failure process of RC structures, the intact concrete between the primary cracks carries part of the resultant tensile force, resulting in the phenomenon known as tension stiffening. Tension stiffening is particularly significant in relatively lightly reinforced members, where the actual stiffness may be several times larger than the stiffness calculated on the basis of fully-cracked cross-sections, where the tensile concrete is ignored and only the embedded tensile reinforcement is taken into consideration. In this paper, a 1-D constitutive model proposed by Long, Zhou and Zhang (2007) is adopted to account for the tension stiffening effect of RC members, where tension stiffening is modeled by adjusting the constitutive relationship for the tensile reinforcement. The stress-strain curve for reinforcing steel is shown in Fig. 13, and the secant modulus of reinforcement E_s is represented as a function of reinforcement strain

$$E_s = \frac{\sigma_z}{\varepsilon_z} = \begin{cases} E_{s0} & (0 < \varepsilon_z < \varepsilon_t) \\ \dfrac{1}{2}\left(E_{s0} + \sqrt{E_{s0}^2 + 4a^2 f_{scr}^2/\varepsilon_z^2}\right) - \dfrac{1-\rho}{\rho\varepsilon_z}\dfrac{\varepsilon_z - \varepsilon_t}{\varepsilon_t - \varepsilon_{tu}} & (\varepsilon_t < \varepsilon_z < \varepsilon_{tu}) \\ \dfrac{1}{2}\left(E_{s0} + \sqrt{E_{s0}^2 + 4a^2 f_{scr}^2/\varepsilon_z^2}\right) & (\varepsilon_{tu} < \varepsilon_z < \varepsilon_y) \\ f_y/\varepsilon_z & (\varepsilon_y < \varepsilon_z) \end{cases}$$

$$f_{scr} = (1/\rho - 1 + n)f_t \qquad n = E_{s0}/E_{c0} \qquad a = \sqrt{(1-d_b)/(1-d_b+nd_b)} \tag{42}$$

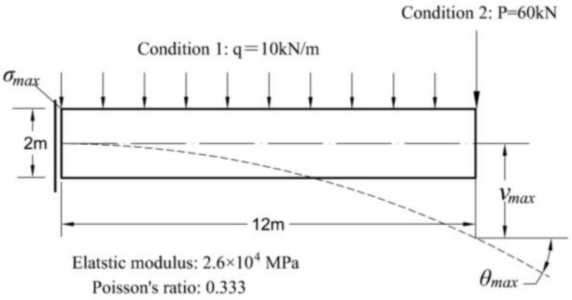

Fig. 14 The adopted cantilever beam

where σ_z and ε_z are the axial stress and axial strain of the steel bars, respectively; E_{s0} is the initial elastic modulus of reinforcement; $\varepsilon_t=f_t\ /E_{c0}$ is the crack initiation strain of concrete, and ε_{tu} is the ultimate strain of concrete, f_y and ε_y are the yield tensile strength and the corresponding strain of the reinforcement, respectively; ρ is the average reinforcement ratio on a single rigid block; d_b is the diameter of a steel bar.

3.5 Convergence procedure

In a nonlinear analysis carried out with a rigid body spring model, the total load applied to the model is divided into a series of load increments. At the completion of each incremental solution, the stiffness matrix of the model is adjusted to reflect nonlinear changes in structural stiffness before proceeding to the next load increment.

The Newton-Raphson approach (Ozcan *et al*. 2009) is adopted in this paper to update the model stiffness. Prior to each solution, the Newton-Raphson approach accesses the out-of-balance load vector, which is the difference between the restoring forces (the loads corresponding to the element stresses) and the applied loads. Subsequently, the program carries out a linear solution using the out-of-balance loads and checks for convergence. If convergence criteria are not satisfied, the out-of-balance load vector is re-evaluated, the stiffness matrix is updated, and a new solution is carried out. The iterative procedure continues until the results converge.

For all numerical models in this paper, the initial load step $F_{initial}$ is chosen as 500 N, while the minimum load step is $F_{initial}/16$. Convergence criterion is based on the out-of-balance loads. The convergence is checked for each load step against the following tolerance condition

$$tolerance=\sqrt{\frac{\sum_{i=1}^{n}\left(\Delta R_i^k\right)^2}{3n}}\leq\eta \tag{43}$$

ΔR_i^k is the out-of-balance load vector of rigid blocks i in the k th step, and n is the total number of blocks. The tolerance limit η is set as 0.5% of the applied loads. To make a compromise between efficiency and accuracy, a maximum iteration number is usually set. This number is here fixed as 200 iterations.

4. Presentation of studied cases

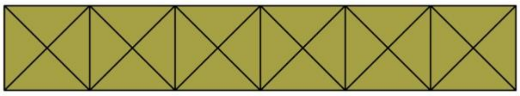

(a) Trianglar mesh n=24

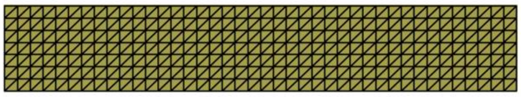

(b) Trianglar mesh n=500

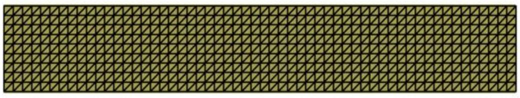

(c) Trianglar mesh n=1000

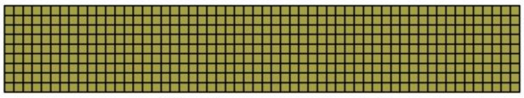

(d) Square mesh n=500

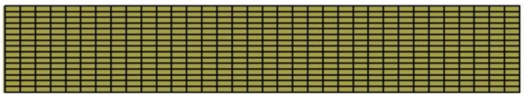

(e) Rectanglar mesh n=500

Fig. 15 Numerical models for the cantilever beam with different mesh sizes and shapes: (a) triangular mesh (n=24); (b) triangular mesh (n=500); (c) triangular mesh (n=1000); (d) square mesh (n=500); (e)rectangular mesh (n=500)

Table 1 Results comparison between numerical models with the same mesh shape (Triangular) and different block numbers

Element Number	Load condition 1				Load condition 2			
	$v_{\max}$ (mm)	Error	$\sigma_{\max}$ (MPa)	Error	$v_{\max}$ (mm)	Error	$\sigma_{\max}$ (MPa)	Error
Analytic solution	1.496	0	1.080	0	1.992	0	1.080	0
Model. a (n=24)	1.446	3.30%	1.081	0.09%	1.900	4.60%	1.081	0.09%
Model. b (n=500)	1.519	1.54%	1.081	0.09%	2.008	0.77%	1.081	0.09%
Model. c (n=1000)	1.523	1.80%	1.081	0.09%	2.015	1.16%	1.081	0.09%

*$v_{\max}$, σ_{max} are the maximum displacement at the cantilever end and the maximum tensile stress at the anchorage end, as shown in Fig. 14.

4.1 Case 1

In order to investigate the effects of mesh size and shape on the numerical results in elastic analyses, a cantilever beam as shown in Fig. 14 is studied. The elastic modulus E_c is equal to 2.6×10^4 MPa and Poisson ratio λ is 0.333. Two loading conditions are chosen, namely uniform loading (q=10 kN/m) and point loading (P=60 kN). The adopted numerical models are shown in Fig. 15. Three comparative numerical models with the same mesh shape (triangular mesh) and different block numbers (respectively being n=24, 500, 1000) are conducted to investigate the effect of mesh size on the numerical results, then two additional numerical models with the same block numbers (being

Table 2 Results comparison between numerical models with the same block number (n=500) and different mesh shapes

Element shape	Load condition 1				Load condition 2			
	v_{max} (mm)	Error	σ_{max} (MPa)	Error	v_{max} (mm)	Error	σ_{max} (MPa)	Error
Analytic solution	1.496	0	1.080	0	1.992	0	1.080	0
Model. b (Triangular)	1.519	1.54%	1.081	0.09%	2.008	0.77%	1.081	0.09%
Model. d (square)	1.507	0.77%	1.081	0.09%	2.015	1.16%	1.081	0.09%
Model. e (rectangular)	1.512	1.03%	1.081	0.09%	2.015	1.16%	1.081	0.09%

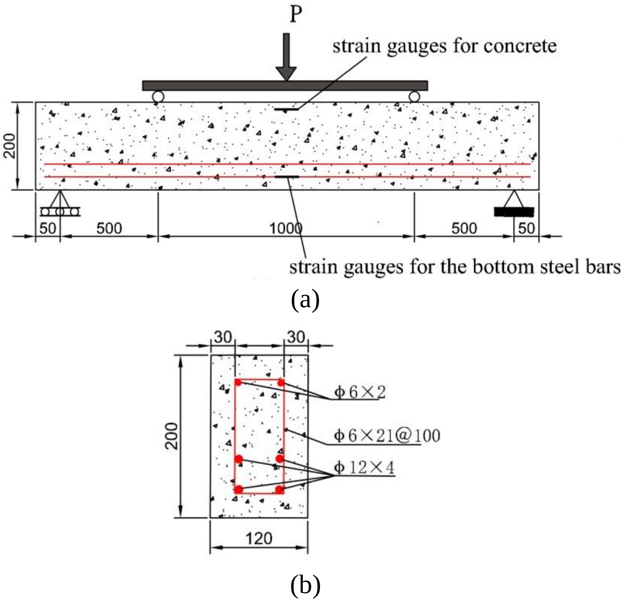

(a)

(b)

Fig. 16 (a) Details of beam geometry; (b) arrangement of reinforcements (mm)

n=500) but different mesh shapes (respectively being square and rectangular mesh) are conducted to investigate the effect of mesh shape on numerical results. The numerical results obtained are shown in Table 1 and Table 2. The comparison result indicates that mesh size and shape have a very limited influence on the maximum displacement at the free end when the block number n is higher than 500, while the calculation accuracy of maximum tensile stress at the anchorage end is not affected by mesh size even when the mesh size is larger.

4.2 Case 2

To further check the performance of the proposed method in failure process analyses, a simply-supported RC beam under two-point loading is adopted herein and corresponding experiment is conducted. The tested beam has a cross section of 200 mm by 120 mm with a clear span of 2000 mm, and the arrangement of steel bars is shown in Fig. 16(b). Loading and supporting arrangements are shown in Fig. 16(a). The test equipment and the loading device are shown in Fig. 17. The stepped loading mode is adopted, and when the experimental load P reaches 10 kN, vertical cracks appear at the bottom of the beam. After that, vertical cracks continue developing. When the load P reaches 45 kN, obvious diagonal cracks are seen in the bending shear regions. When the load P exceeds 90.4 kN, the beam fails and the crack pattern is shown in Fig. 18. During the loading process, the mid-section deflection are precisely measured at every load increment of 5 kN by the dial gauge at the mid-span until the load P reached its maximum, then the load P is recorded at every displacement increment of 1.5 mm. The load-deflection curve is shown in Fig. 19. The compressive strain of concrete and the tensile strain of the bottom steel bars of mid-section are measured by strain gauges in Fig. 16(a), and the load-strain responses are

Fig. 17 The test equipment and the loading device

Fig. 18 Crack pattern obtained by experiment

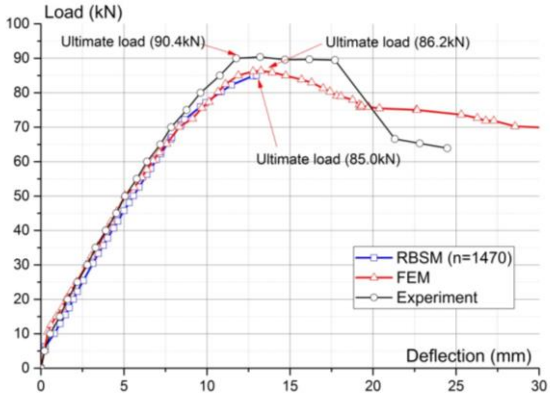

Fig. 19 Comparison between numerical and experimental results

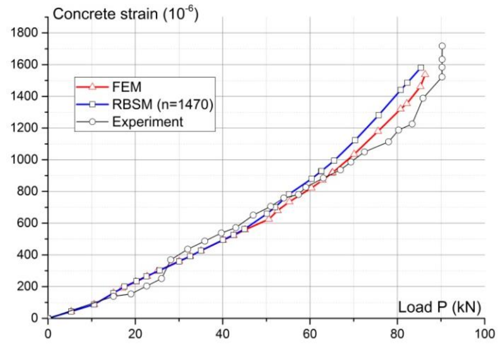

(a) concrete compressive strain

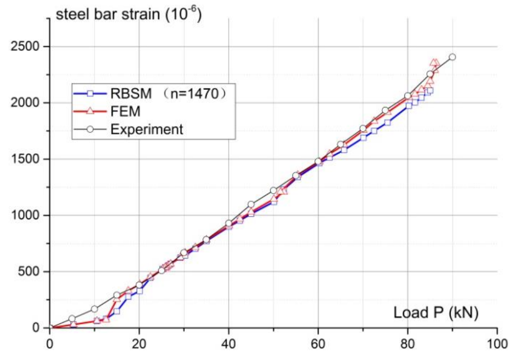

(b) reinforcement tensile strain

Fig. 20 Load-strain responses at mid-span cross-section predicted by different methods

plotted in Figs. 20(a), (b), respectively.

Three rigid body spring models with different block numbers (respectively being *n*=4000, 1470, 624) are developed for the tested beam to investigate the effect of mesh size on the numerical results in failure analyses, as shown in Fig. 21. The material properties of the concrete and reinforcement adopted in the model are listed in Table 3. The proposed convergence procedure is adopted to approach the ultimate bearing capacity of the beam. The final crack patterns and load-deflection responses from rigid body spring models with different element numbers are plotted in Fig. 22 and Fig. 23, respectively. The load-deflection responses from the rigid body spring model (*n*=1470) are compared with the experimental result in Fig. 19. The concrete compressive strain ε_n of the interface 1939 in Fig. 21(a) is presented in Fig. 20(a), and the reinforcement tensile strain ε_z of the interface 626 in Fig. 21(a) is presented in Fig. 20(b).

Table 3 Material properties adopted in rigid body spring models

f_t (MPa)	f_c (MPa)	E_{c0} (GPa)	c (MPa)	φ	f_y (MPa)	E_{s0} (GPa)	G_f (N/ m)
2.2	23.4	31.5	4.5	62.5°	420	195	100

*c, φ are determined according to the experiment conducted by Cong *et al*. (2015).

Table 4 Constitutive parameters adopted in the concrete damage plastic model

θ	e	f_{b0}/f_c	K_c
38°	0.1	1.12	0.666

*θ is the dilation angle; e is the flow potential eccentricity of the plastic potential surface; f_{b0} / f_c is the ratio of the initial equibiaxial compressive yield stress to the initial uniaxial compressive yield stress; K_c is the ratio of the second stress invariant on the tensile meridian to that on the compressive meridian.

For comparison, a finite element model (FEM) is developed for the tested beam using the ABAQUS program. ABAQUS has been widely used in both engineering and academic areas to predict complicated behavior of RC structures with high credibility (Jankowiak and Lodygowski 2005). In the present work, eight-node solid elements (C3D8R) are used to model the concrete, and internal reinforcement is modeled by 3D truss elements (T3D2). The FEM model consists of 2115 nodes, 1986 concrete elements and 546 reinforcement elements, as shown in Fig. 24. The concrete damage plasticity model is adopted to simulate the complete inelastic behavior of concrete in

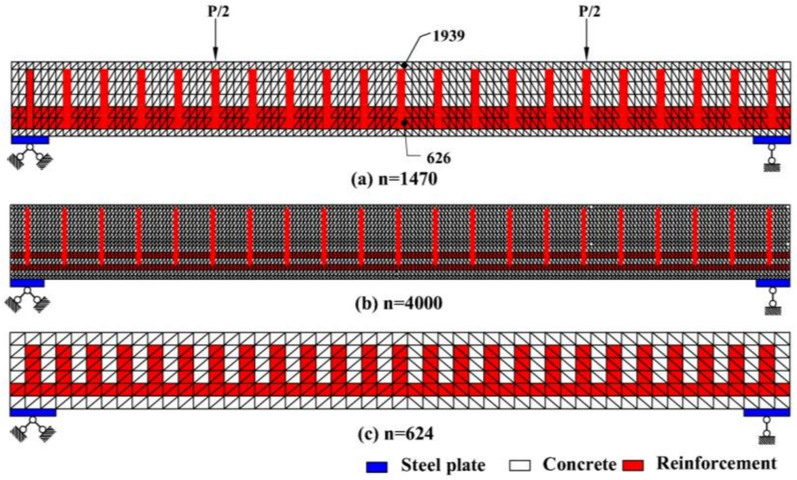

Fig. 21 Rigid body spring models with different block numbers: (a) block number *n*=1470; (b) block number *n*=4000; (c) block number *n*=624

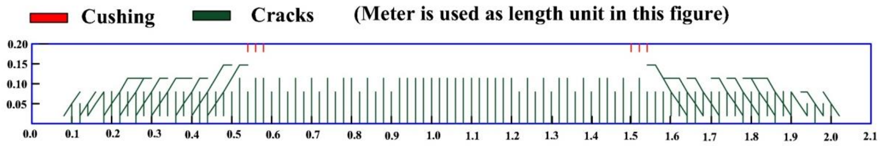

(a) n=1470

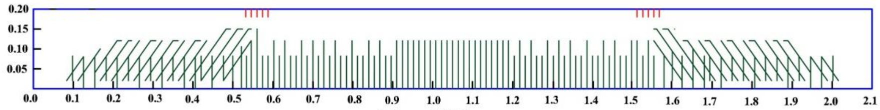

(b) n=4000

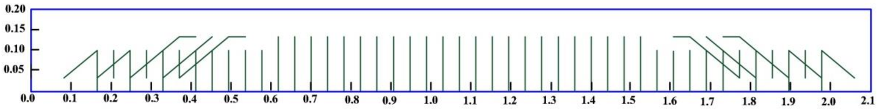

(c) n=624

Fig. 22 Crack patterns obtained by rigid body spring models with different block numbers: (a) block number n=1470; (b) block number n=4000; (c) block number n=624

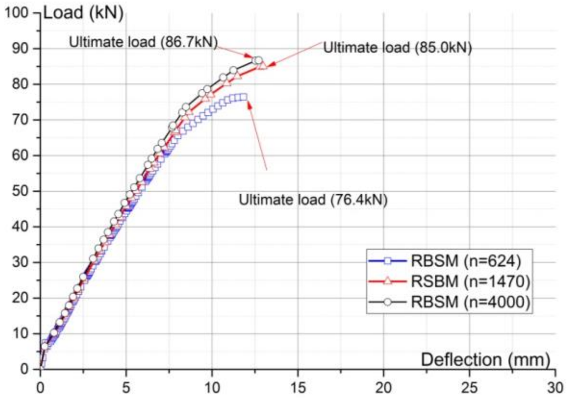

Fig. 23 Load-deflection curves obtained by rigid body spring models with different block numbers (being n=624, 1470, 4000)

compression and tension, and the constitutive parameters are determined according to Jankowiak and Lodygowski (2005), and are summarized in Table 4. Steel bars are assumed to be an elastic-perfectly plastic material model which is identical in tension and compression, and perfect bond between the concrete and internal reinforcement is assumed. Basic material properties for the concrete and steel reinforcement are listed in Table 3. The load-deflection response of the tested beam predicted by FEM is plotted with the RBSM and experimental results in Fig. 19. The concrete compressive strain ε_n of element 1470 in Fig. 24 is presented in Fig. 19(a), and the reinforcement tensile strain ε_z of element 120 in Fig. 24 is presented in Fig. 19(b).

The ultimate loads and load-deflection curves of the tested beam predicted by the proposed method, experiment and FEM are close to each other as shown in Fig. 19. The mesh size of rigid body spring models has slight influence on the numerical results when the block number is larger than 1470, as shown in Fig. 23.

Figs. 18 and 22 show that the crack characteristics of the tested beam, such as the location, height, dip angle and development trend, predicted by the proposed method are in good agreement with the experimental results, but the mesh size of rigid body spring models has some impact on numerical crack spacing. Numerical crack spacing reported in Fig. 22 is indeed much narrower than that of experimental results. One possible cause is that perfect bond between the concrete and steel reinforcing is assumed in numerical simulations, but the assumption would not be true for the tested beam.

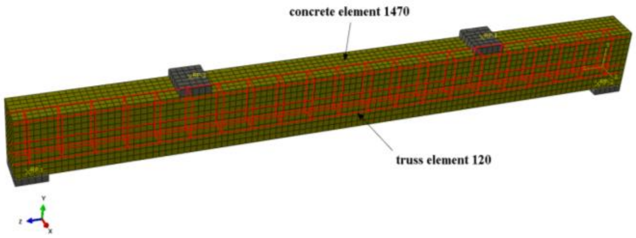

Fig. 24 Finite element model for the tested beam

Figs. 20(a)-(b) show that the reinforcement strains and concrete compressive strains obtained from three different methods are in good agreement.

5. Conclusions

This paper presents a modified rigid body spring method for simulating the failure process of reinforced concrete structures. The mesh sensitivity and effectiveness of the proposed method are firstly verified by elastic analyses on a cantilever beam under different loading conditions, then the method is applied to analyze the failure process of a RC beam under two-point loading. As confirmed by comparisons with the experimental data and FEM results, it can be concluded that:

- Mesh size and mesh shape have limited influence on numerical results in both elastic and nonlinear analyses when the block number of rigid body spring models is higher than 1470, and the proposed method has high accuracy for the calculation of element stress even when the mesh size is larger. Mesh sizes of rigid body spring models have some impact on numerical crack spacing, and one possible cause is that perfect bond between the concrete and steel bars is assumed in numerical simulations, but the assumption would not be true for the tested beam.

- The proposed method can successfully predict the load-deflection response, ultimate strengths, cracking patterns of reinforced concrete components, and is able to provide some physical characteristics of cracks, such as the location, height, dip angle and development trend, which makes it a feasible and competitive method in simulating the failure process of RC structures.

Acknowledgments

The research described in this paper is financially supported by the Natural Science Foundation of China (51678253, 41472259) and National Key Research and Develop Program of China (2016YFC080250504). These supports are gratefully acknowledged.

References

Aoyagi, Y. and Yamada, K. (1983), "Strength and deformation characteristics of reinforced concrete shell elements subjected to in-plane forces", *Proc. JPN Soc. Civil Eng.*, **331**, 167-180.

Barzegar, F. and Maddipudi, S. (1997), "Three-dimensional modeling of concrete structures. II: reinforced concrete", *J. Struct. Eng.*, ASCE, **123**(10), 1347-1356.

Belytschko, T. and Black, T. (1999), "Elastic crack growth in finite elements with minimal remeshing", *Int. J. Numer. Meth. Eng.*, **45**(5), 601-620.

Belytschko, T., Krongauz, Y., Fleming, M., Organ, D. and Liu, W.K.S. (1996), "Smoothing and accelerated computations in the element free Galerkin method", *J. Comput. Appl. Math.*, **74**(1-2), 111-126.

Bernardi, P., Cerioni, R., Michelini, E. and Sirico, A. (2015), "Numerical modeling of the cracking behaviour of RC and SFRC shear-critical beams", *Eng. Fract. Mech.*, **167**, 151-166.

Burns, S.J. and Hanley, K.J. (2017), "Establishing stable time-steps for DEM simulations of non-collinear planar collisions with linear contact laws", *Int. J. Numer. Meth. Eng.*, **110**, 186-200.

Carter, B.J., Wawrzynek, P.A. and Ingraffea, A.R. (2000), "Automated 3-D crack growth simulation", *Int. J. Numer. Meth. Eng.*, **47**(1), 229-253.

Cong, Y., Kong, L., Zheng, Y.R., Erdi, A.B. and Wang, Z.Q. (2015), "Experimental study on shear strength of concrete", *Concrete*, **5**, 40-45.

Guo, N. and Zhao, J.D. (2014), "A coupled FEM/DEM approach for hierarchical multiscale modelling of franular media", *Int. J. Numer. Meth. Eng.*, **99**(11), 789-818.

Jankowiak, T. and Lodygowski, T. (2005), "Identification of parameters of concrete damage plasticity constitutive model", *Found. Civil Environ. Eng.*, **6**, 53-69.

Jin, C., Soltani, M. and An, X.H. (2005), "Experimental and numerical study of cracking behaviour of openings in concrete dams", *Comput. Struct.*, **83**(8), 525-535.

Kawai, T. (1977). "New element models in discrete structural analysis", *J. Soc. Naval Arch. JPN*, **141**(2), 187-193.

Li, M.G., Yu, H.T., Wang, J.H. and Chen, J.J. (2015), "A multiscale coupling approach between discrete element method and finite difference method for dynamic analysis", *Int. J. Numer. Meth. Eng.*, **102**(1), 1-21.

Long, X. and Lee, C.K. (2015) "Modelling of two dimensional reinforced concrete beam-column joints under monotonic loading", *Adv. Struct. Eng.*, **18**(9), 1461-1474.

Long, X. and Lee, C.K. (2015), "Improved strut-and-tie method for 2D RC beam-column joints under monotonic loading", *Comput. Concrete*, **15**(5), 807-831.

Long, X., Bao, J.Q., Tan, K.H. and Lee, C.K. (2014) "Numerical simulation of reinforced concrete beam/column failure considering normal-shear stress interaction", *Eng. Struct.*, **74**, 32-43.

Long, X., Tan, K.H. and Lee, C.K. (2013), "A 3D co-rotational beam element for steel and RC framed structures", *Struct. Eng. Mech.*, **48**(5), 587-613.

Long, X., Tan, K.H. and Lee, C.K. (2014) "Bond stress-slip prediction under pullout and dowel action in reinforced concrete joints", *ACI Struct. J.*, **111**(4), 977-988.

Long, Y.C., Zhou, Y.D. and Zhang, C.H. (2007), "Reinforcement stiffening model for reinforced concrete interaction effects", *J. Tsinghua Univ. (Sci. & Tech.)*, **47**(6), 793-796.

Ottosen, N.S. (1980), "Constitutive model for short-time loading of concrete", *J. Eng. Mech. Div.*, **105**(1), 127-141.

Ozcan, D.M., Bayraktar, A., Sahin, A., Haktanir, T. and Turker, T. (2009), "Experimental and finite element analysis on the steel fiber-reinforced concrete (SFRC) beams ultimate behaviour", *Constr. Build. Mater.*, **23**, 1064-1077

Saito, S. and Hikosaka, H. (1999), "Numerical analyses of reinforced concrete structures using spring network models", *J. Mater. Concrete Struct., Pavem.*, JSCE, **44**(627), 289-303.

Shi G.H. (1988), "Discontinuous deformation analysis: a new numerical model for the statics and dynamics of block systems", Ph.D. Dissertation, University of California at Berkeley, Berkeley.

Shi G.H. (1994), "Modeling dynamic rock failure by discontinuous deformation analysis with simplex integrations", *Proceedings of the 1st North American Rock Mechanics Symposium*, Austin, Texas, July.

Sirico, A., Michelini, E., Bernardi, P. and Cerioni, R. (2017), "Simulation of the response of shrunk reinforced concrete elements subjected to short-term loading: a bi-dimensional numerical approach", *Eng. Fract. Mech.*, **174**, 64-79.

Soroushian, P., Obaseki, K. and Rojas, M.C. (1987), "Bearing strength and stiffness of concrete under reinforcing bars", *ACI Mater. J.*, **84**(3), 179-184.

Tang, G.B. and Xiang, Y.Q. (2015), "Mechanical properties and numerical simulation of crack interface in reinforced concrete", *Shuilixuebao*, **46**, 42-50.

Vecchio, F.J. and Shim, W. (2004), "Experimental and analytical re-examination of classic concrete beams", *J. Struct. Eng.*, ASCE, **130**(3), 460-469.

Vecchio, F.J., Bentz, E.C. and Collins, M.P. (2004), "Tools for forensic analysis of concrete structures", *Comput. Concrete*, **1**(1), 1-14.

Wang, Y.F. and Zhang, Q. (2009), "Analysis of anti-sliding stability in deep foundation of Xiangjiaba gravity dam based on interface element method", *Rock Soil Mech.*, **30**(9), 2691-2696.

Yao, C., Shao, J.F., Jiang, Q.H. and Zhou, C.B. (2016), "Numerical study of excavation induced fractures using an extended rigid block spring method", *Comput. Geotech.*, **85**, 368-383.

Zhang, Q., Wang, Z.Q. and Xia, X.Z. (2012), "Interface stress element method and its application in analysis of anti-sliding stability of gravity dam", *Sci. China Technol. Sci.*, **55**(12), 3285-3291.

CC